BNL-209521-2018-PUCP

Visualization and Quantum Computation of Moire Superconductivity in Bilayer Graphene, Carbon Nanocones and Nanostrips

S. Elghazoly, M. McGuigan

Submitted to the 2018 New York Scientific Data Summit (NYSDS): Data-Driven Discovery in Science and Industry Conference
to be held at Upton, NY
August 06 - 08, 2018

September 2018

Computational Science Initiative

Brookhaven National Laboratory

U.S. Department of Energy

USDOE Office of Science (SC), Advanced Scientific Computing Research (SC-21)

This work was supported by the Laboratory Directed Research and Development Program of Brookhaven National Laboratory under U.S. Department of Energy Contract No. DE-SC0012704.

DISCLAIMER

Visualization and quantum computation of Moiré superconductivity in bilayer graphene, carbon nanocones and nanostrips

Sarah Elghazoly
Physics, Smith College
Northampton, MA 01063
elghazoly97@gmail.com

Michael McGuigan
Computational Science Initiative
Brookhaven National Laboratory
Upton, NY 11973
mcguigan@bnl.gov

***Abstract*—The purpose of this project is to visualize and study the electronic properties of carbon nanostructures. The principal structures studied are AA and AB (Bernal) stacked graphene bilayers, an 80C nanocone with pentagonal defects at its apex, and a 16C nanoring. Graphene and other based nanostructures have attracted much attention due to their unique electronic properties. For example, bilayer graphene shows superconductivity at certain magic angles of rotation. Open source molecular modeling and visualization programs like SAMSON, Avogadro, and VMD are utilized to generate the structures above. Using bond information in order to find nearest neighbors, an adjacency matrix can be generated from which the energy eigenvalues are solvable and are used to visualize the dispersion relation, free energy, persistent current, Green's function, and entanglement entropy. The goal of this project is to study the effect of rotation on the electronic properties of bilayer graphene, particularly as it pertains to the magic angle where superconductivity occurs, as well as the electronic properties of the bilayer Moiré patterns which emerge due to the superposition of the identical lattices at different angles. An important goal is to incorporate phonon interactions into the tight-binding model for carbon structures, and to utilize quantum based computing as a tool to find the ground state properties of these structures, particularly in the terminating case where boundary conditions have an effect.**

***Index Terms*—Graphene, Green's Function, Moir patterns, IBM QISKit, Variational Quantum Eigensolver**

I. Nanostructure Visualization

The physical properties of carbon-based systems are largely determined by their dimensionality. As such, it is important to understand a nanostructure's geometry and topology particularly as it affects electron transport and phonon interaction. Using the open-source molecular modeling and visualization softwares Software for Adaptive Modeling and Simulation Of Nanosystems (SAMSON) v. 0.7.0, Avogadro v. 1.2.0 [1], and Visual Molecular Dynamics (VMD) [2] [3] enabled the visualizations of nanostructures, some of which are natural and experimentally grown, and some of which are avenues for further research into the topology of lattice structures in order to develop theories on how the electronic properties might be affected in carbon-based devices with similar characteristics. Such characteristics include defects in the hexagonal lattice that creates curvature in the 2D form of graphene, or the superposition of two structures and the relative angle between them, or even how atom arrangement at the edges affects the electronic properties of a lattice.

A. Moiré Superconductor

Since its isolation from graphite in 2004, a carbon-based structure that has been the subject of extensive solid-state physics research is graphene [4] [5]. Single layer graphene (SLG) is a sheet a single atom thick formed of a lattice of hexagonally arranged sp^2 hybridized carbon atoms, called a honeycomb lattice. Each carbon atom has six electrons and an electrical configuration $1s^2 2s^2 2p^2$. The hybridization of the 2s an 2p orbitals lowers the system's energy when covalent bonds between carbon atoms take place. The hybridization involves three of the four valence electrons in the carbon atom, leaving a single electron perpendicular to the graphene plane in the p_z orbital [6]. The electronic properties of graphene are owed to the valence (π) band given by the p_z orbital. The lattice structure of graphene can be seen as being composed of two triangular sublattices with two atoms per unit cell. The two points K and K$'$ at the corner of the Brillouin zone (BZ) of graphene 1 are known as the Dirac points, behave as low energy Dirac relativistic fermions where the energy bands meet, and the energy spectrum is approximately linear. The dispersion relation of SLG for nearest and next nearest hopping is given by Eqn 1, where t and t' are the nearest neighbor and next-nearest neighbor hopping parameters with experimental values of 2.7 eV and 0.4 eV respectively, and k_x, k_y are the wave vectors, and a is the lattice constant of graphene, approximately 0.246 nm.

$$\begin{aligned} E^{\pm}(k) &= \pm t\sqrt{3+f(k)} - t' f(k) \\ f(k) &= 2\cos\sqrt{3}k_y a + 4\cos\frac{\sqrt{3}k_y a}{2}\cos\frac{3k_x a}{2} \end{aligned} \tag{1}$$

The dispersion relation gives the level of all possible energies and momenta for a material. The dispersion relation of graphene is approximately linear near the Fermi level and can be described by the pseudo-relativistic Dirac equation - a relativistic wave equation that describes spin $\frac{1}{2}$ massive particles [7].

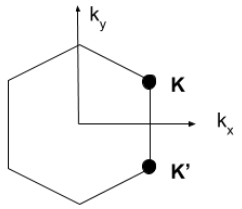

Fig. 1: Brillouin zone of graphene with non-equivalent Dirac points K and K′.

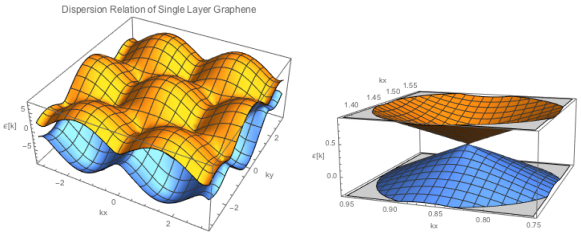

(a) Dispersion of SLG (b) Dispersion Near Dirac

Fig. 2: a) Dispersion relation of SLG b) Dispersion relation of SLG near Dirac Point for low energy-states, showing Dirac cone which allows electrical conduction to be described by the Dirac equation

In bilayer graphene there are two methods of stacking: AA and AB (Bernal) stacking. AA stacking is a direct superimposition of the top layer over the bottom layer, where the A atoms of the top layer are directly over the A atoms of the lower layer. In Bernal stacking, which is more commonly encountered and electrically stable, the top layer is offset by the length of one carbon-carbon bond.

Exposing stacked graphene layers to a perpendicular electric field can induce a tunable band gap, important for its potential uses in electronics.

Rotated Bernal stacked graphene has recently shown superconductivity at certain magic angles of rotation . Researchers have found that for an angle of approximately 1.1 degree tunable superconductivity can be achieved in doped graphene at temperatures as high as 1.7 K [8].

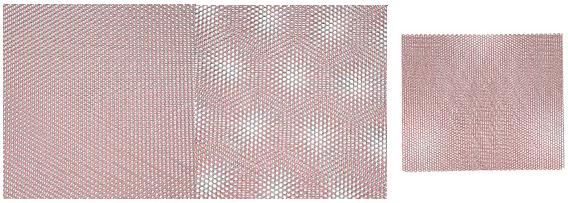

(a) AB Stacked Graphene Unrotated (b) AB Stacked Graphene Rotated by Some θ (c) AB Stacked Graphene at Magic Angle 1.1

Fig. 3: Visualizations made using Avogadro and VMD a) 24 atom Möbius strip b) 16 atom ring

(a) N=24 Möbius strip (b) N=16 Nanotube

Fig. 4: Visualizations made using Avogadro and VMD a) 24 atom Möbius strip b) 16 atom ring

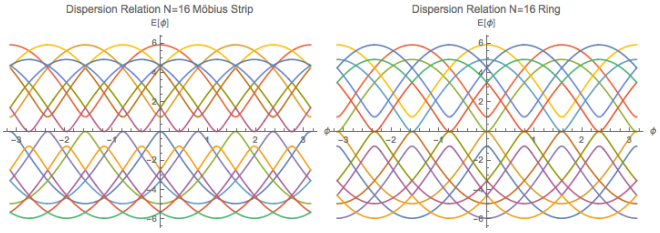

(a) N=16 Möbius strip (b) N=16 Nanostrip Ring

Fig. 5: a) Energy dispersion of 16 atom Möbius strip b) 16 atom ring

B. Polyacetelyne, Nanorings and Nanostrips

The Su-Schrieffer-Heeger polyacetylene (SSH) model has also been extensively researched to characterize electric properties on a 1D lattice, due to its conductivity as an organic polymer [9]. The presence of phonon-electron interaction in the SSH model causes dimerization of the lattice and an electronic excitation at zero energy.

A ring of carbon atoms is very similar to the SSH model, with the added advantage that the influence of flux due to a magnetic field can be analyzed and the persistent current of the model can be calculated. Additionally, the ring is a finite case and easily given an adjacency matrix using the approach from [10] [11].

The dispersion relation for a ring of N atoms with a flux ϕ as shown in the figure 6 is given by $E_n(\phi) = 2\cos(\frac{2\pi n}{N} + \phi)$

Stacking the rings or atoms and connecting the adjacent atoms gives a round nanostrip of graphene. Nanostrips area terminated case of graphene where the boundary conditions play an important role in the electronic spectrum of the

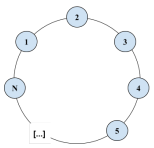

Fig. 6: Ring of N atoms.

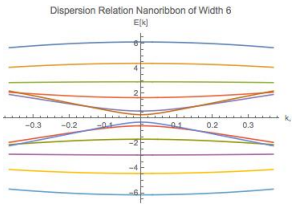

Fig. 7: Dispersion of a nanoribbon with a width of 6 unit cells

(a) A (b) B

Fig. 8: Pentagonal Nanocones created using Avogadro and rendered with VMD

nanostructure. In the case of graphene nanoribbons, there are two cases of carbon arrangement along terminating edges. Edge-localized states are found in zigzag-edge graphene, and armchair graphene nanostrips have one electron band gaps [7].

C. Stacked Nanocone

Graphene cones which have been experimentally produced are pentagonal defects in 2D graphene sheets. Graphitic cones are important avenues for research because of the importance of electronic effects due to defects in the development of carbon based electronics, and the possible implementation of curved carbon structures [12]. Graphene cones formed from pentagonal defects on a graphene lattice show distinct low-energy electronic properties at the apex due to the topological differences that change the electron transport properties [13] [14].

Superimposing two graphene cones and performing rotations, as in the case of AA rotated bilayer graphene, may yield unique electronic properties as yet unexplored.

Nanocones with an apex containing several pentagons was studied in [15]. These nanocones or nanohorns are a promising material for developing bio and chemical sensors due to their high conductivity and high current capacity, as well as stability.

D. Nanohorn

A different type of nanohorn modeled in figure 10 has 10 pentagons and 5 heptagons to create a bulbous shape on a nearly planar surface. The inspiration for this model is the vortex model that joins a carbon nanotube to a plane of graphene. The nanohorn has an Euler characteristic of 1. For more information on carbon nanohorns see [15],

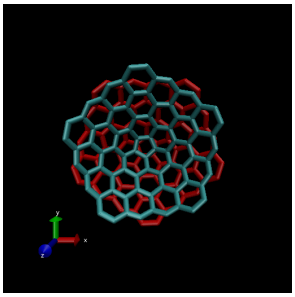

Fig. 9: Two overlaid cones with one cone rotating with respect to the other in the VMD animation environment. View from underneath the cones.

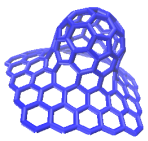

Fig. 10: Nanohorn created using Avogadro and rendered in VMD.

E. Euler Formula

In topology, the Euler characteristic is a number that describes the topology of a structure classically defined as the number of faces of a polyhedron added to the difference between the number of edges and vertices.

$$V - E + F \tag{2}$$

In the disc formed from a section of graphene, the Euler characteristic is $24 - 30 + 7 = 1$ consistent with a circular disk.

For the N = 24 ring formed by hexagons the Euler characteristic is $24 - 30 + 6 = 0$ consistent with that of a circle, torus or möbius strip. The N = 24 möbius strip formed from hexagons also has an Euler characteristic of 0.

The nanocone formed by a single pentagonal defect surrounded by 5 hexagons has an Euler characteristic of $20 - 25 + 6 = 1$.

Finally, a nanohorn as shown in figure 10 has an Euler characteristic of $155 - 220 + 66 = 1$.

II. Computation

A. Tight Binding Model

Quantum field theory (QFT) is a unifying mathematical framework for special relativity and quantum mechanics, extending quantum mechanics dealing of particles to systems with infinite degrees of freedom. (Ortega, Calabrese, Drissi)

The tight binding model approach is a QFT method for calculating electronic band structures based on the couplings

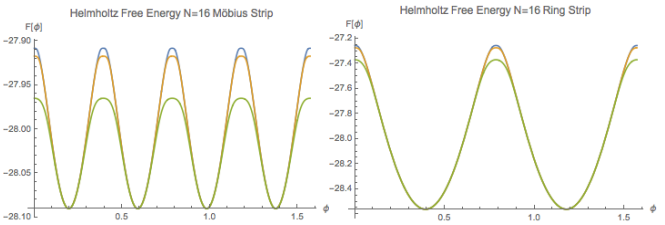

(a) Helmholtz Free Energy Möbius Strip (b) Helmholtz Free Energy N=16 Ring

Fig. 11: a) Helmholtz Free Energy of 16 atom Möbius strip. b) Helmholtz Free Energy of 16 atom ring strip

between neighboring atomic states in a molecule. For graphene and sp2 hybridized carbon atoms, the orbital of interest is the pz orbital.

For simple explanations of the derivation of the tight binding model of graphene look to references [6]

B. Free energy, flux and chemical potential

The Helmholtz Free Energy of a linear system [16] is given by the equation [10]

$$\begin{aligned} F &= -kT\ln(2\sinh\tfrac{\omega_i}{2kT}) \\ &= -kT\textstyle\sum_i \ln(1-\exp(-\omega_i/kT)) - \frac{1}{2}\sum_i \omega_i \end{aligned} \tag{3}$$

where $\hbar$ is set to 1. Here, ω_i is the ith dispersion relation and k is the Boltzmann constant.

$$F_{ferm,bos} = \pm kT\sum_i \ln(1\pm\exp(-\omega_i/kT)) \tag{4}$$

In Figures 11a and 11b, the Helmholtz free energies of the Möbius strip and nanostrip ring are shown for various temperatures. These graphics were modeled using Mathematica.

C. Propagator, time, temperature and chemical potential (real time formulation)

The propagator, commonly known as Green's functions is a function in QFT that gives the probability amplitude for a particle to travel from one place to another.

1) D greater, D lesser boson: Functional Integral Formulation of real-time thermal field theory [17]

D greater

$$\begin{aligned} D_>(x) &= \int\Big[\tfrac{d^3k}{(2\pi)^2 2E}[e^{i(k\cdot x-(E-\mu)t)}[1+n(E-\mu)]] \\ &+ \qquad e^{i(-k\cdot x+(E+\mu)t)}n(E+\mu)\Big] \end{aligned} \tag{5}$$

D lesser

$$\begin{aligned} D_<(x) &= \int\Big[\tfrac{d^3k}{(2\pi)^2 2E}[e^{i(k\cdot x-(E-\mu)t)}[n(E-\mu)]] \\ &+ \qquad e^{i(-k\cdot x+(E+\mu)t)}[1+n(E+\mu)]\Big] \end{aligned} \tag{6}$$

Where $n(w)=\frac{1}{e^{\beta w}-1}$ and β is inverse temperature.

For the discrete case and fixed position x:

$$\begin{aligned} D_>(t) &= \textstyle\sum_k \frac{1}{2E_k}\big[e^{-i(E_k-\mu)t}[1+n(E_k-\mu)] \\ &+e^{i(E_k+\mu)t}[n(E_k+\mu)]\big] \end{aligned} \tag{7}$$

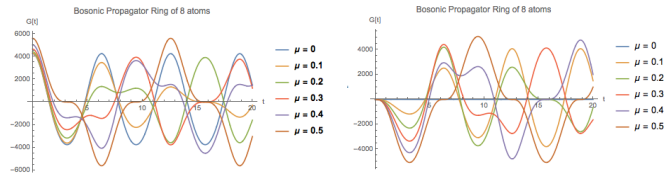

(a) Real Part (b) Imaginary Part

Fig. 12: Real and Imaginary parts of the boson propagator of a carbon nanoring for fixed position x =0.

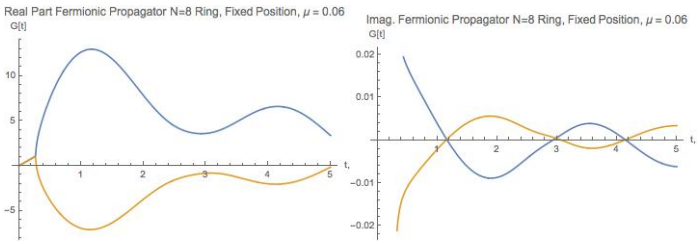

(a) Real Part (b) Imaginary Part

Fig. 13: Real and Imaginary parts of the fermion propagator of a carbon nanoring for fixed position x = 0.

$$\begin{aligned} D_<(t) &= \textstyle\sum_k \frac{1}{2E_k}\big[e^{-i(E_k-\mu)t}[n(E_k-\mu)] \\ &+e^{i(E_k+\mu)t}[1+n(E_k+\mu)]\big] \end{aligned} \tag{8}$$

In Figures 12a and 12b the real and imaginary parts of the boson propagator of a carbon nanoring were plotted for various chemical potentials at a fixed position.

2) D greater, D lesser fermion:

$$\begin{aligned} S(x,y) &= (-i\gamma\cdot\partial - m)\int\Big[\tfrac{d^3p}{(2\pi)^3 2iE_p}[e^{i\mathbf{p}\cdot(\mathbf{x}-\mathbf{y})} \\ &\cdot\Big(\theta(x_o,y_o)[\tfrac{e^{-iE_p(x_o-y_o)}}{1+e^{-\beta(E_p+\mu)}} - \tfrac{e^{-\beta(E_p+\mu)+iE_p(x_o-y_o)}}{1+e^{-\beta(E_p+\mu)}}] \\ &+\theta(y_o,x_o)[\tfrac{e^{-iE_p(x_o-y_o)}}{1+e^{-\beta(E_p+\mu)}} - \tfrac{e^{-\beta(E_p-\mu)-iE_p(x_o-y_o)}}{1+e^{-\beta(E_p-\mu)}}]\Big) \end{aligned} \tag{9}$$

where x_o is the at some time, and y_o is the final time, and the vectors **x** and **y** are position vectors. [18] [19]

The discretized form used for the ring of atoms is

$$\begin{aligned} D_>fermion &= (-i\gamma\partial - m) \\ &\textstyle\sum_n \frac{e^{k\cdot x}}{2iE_n}\Big[\frac{e^{-iE_nt}}{1+e^{-\beta(E_n-\mu)}} - \frac{e^{-\beta(E_n+\mu)+iE_nt}}{1+e^{-\beta(E_n+\mu)}}\Big] \end{aligned} \tag{10}$$

$$\begin{aligned} D_<fermion &= (-i\gamma\partial - m) \\ &\textstyle\sum_n \frac{e^{k\cdot x}}{2iE_n}\Big[\frac{e^{E_nt}}{1+e^{-\beta(E_n+\mu)}} - \frac{e^{-\beta(E_n-\mu)-iE_nt}}{1+e^{-\beta(E_n-\mu)}}\Big] \end{aligned} \tag{11}$$

and is plotted for fixed position in Figures 13a and 13b

D. Entanglement Entropy

Entanglement entropy is a measure of quantum entanglement in quantum many-body entangled states. Entanglement entropy can be used to characterize quantum phases of matter,

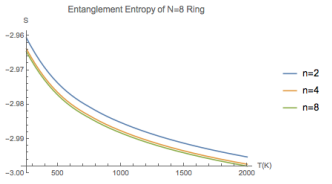

(a) Entanglement Entropy N=8 Ring

Fig. 14: Entanglement entropy of a N=8 ring as a function of temperature for different subsets n of the total ring.

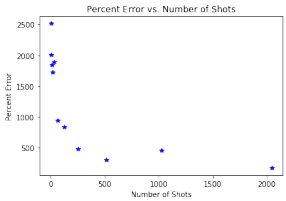

Fig. 15: Percent error of quantum simulation of ground state energy of SSH model vs number of shots.

critical phenomena, and dynamics in quantum systems in QFT. Entanglement entropy is defined as the von Neumann entropy $S_A = -\mathrm{Tr}\rho_A \ln \rho_A$, where A is a subsystem with reduced density matrix ρ_A.

Using methods described in [11] for a massive fermion on a discretized circular lattice, the entanglement entropy can be plotted as a function of temperature of a N=8 ring. The discretized Hamiltonian is given by

$$H = \sum_{j=1}^{N} \left[\frac{-i}{2}(\Psi_j^\dagger \sigma^3 \Psi_{j+1} - \Psi_{j+1}\sigma^3\Psi_j) + ma\Psi_j^\dagger \sigma^1 \Psi_j \right] \quad (12)$$

with anti-commutation relation $\{\Psi_j, \Psi_k^\dagger\} = \delta_j k$.

The two point correlation function of two Ψ fields are components of the matrix C, the eigenvalues of which have a one to one correspondence with the eigen-energies of a reduced energy matrix written as a free-particle Hamiltonian.

$$\begin{aligned} \langle \Psi_j \Psi_k^\dagger \rangle &= \frac{1}{2L}\sum_{a=1}^{N} \left[(1 + \frac{\sinh(\beta\mu)}{\cosh(\beta\mu)+(-1)\cosh(\beta\omega(\theta_a))}) \right. \\ &+ \left. (\frac{\sin(\theta_a)}{\omega(\theta_a)\epsilon}\sigma_3 + \frac{m}{\omega(\theta_a)}\sigma_1) \frac{\sinh(\beta\omega(\theta_a))}{(-1)\cosh(\beta\mu)+\cosh(\beta\omega(\theta_a))} \right] \end{aligned} \quad (13)$$

where β is inverse temperature, μ is chemical potential, $\epsilon = L/N$, ω is the dispersion relation of a ring given by $\omega(\theta_a)^2 = m^2 + \frac{\sin^2(\theta_a)}{\epsilon^2}$, for $\theta_a = \frac{2\pi a}{N}$, and σ_1 and σ_3 are the first and third Pauli matrices.

The entanglement entropy of the carbon nanoring for different subsets of a carbon nanoring is shown in Figure 14a.

III. Quantum Computation

Quantum simulations of the Su-Schrieffer Heeger model were performed using IBM's Quantum Experience Package, using the Quantum Information System Kit (QISKit) and QISKit Acqua. The IBM QISKit is an open-source quantum computing platform that gives users access to five-qubit quantum processors through the cloud. Using Jupyter notebook as the code interface for the quantum computer, Python scripts can operate the quantum computing platform.

A. Tight binding model with phonon interaction

B. Phonon interaction

Electron-phonon interaction is important for the creation of phonon scattering of electrons. Phonons create the vibrational modes on the lattice and affect heat capacity, thermal expansion and electrical conductivity.

The Su-Schrieffer Heeger (SSH) model for polyacetylene is a simple, one-dimensional (1D) case of a topological insulator [20]. Polyacetylene is a chain consisting of N unit cells of carbon atoms with alternating double and single bonds.

A topological insulator has the characteristic of being an insulator in the interior, and conducting on the surface. The dimensionality and topology in the determination of the electronic characteristics of a topological insulator. The SSH model models spinless-fermions on a one dimensional lattice with a hopping parameter. Electron-phonon interactions play an important role in quantum systems and in polymers the hopping of electrons along chain is moderated strongly by lattice vibrations.

The Hamiltonian of the SSH model, neglecting spin, is given by:

$$\begin{aligned} H_{SSH} &= -\textstyle\sum_i t_{i+1,i}(c_{i+1}^\dagger c_i + \text{H.c.}) \\ &\quad + \frac{K}{2}\textstyle\sum_i (u_{i+1}-u_i)^2 + \frac{M}{2}\sum_i \dot{u_i}^2 \end{aligned} \quad (14)$$

where c_i ($c_i^\dagger$) are the fermion creation (annihilation) operators at site i, and u is the boson field.

Considering the case where the hopping parameter, t, is the same for all sites i, and u is dimerized such that $u_i = (-1)^i u$ as in [21], the Hamiltonian is reduced to

$$\begin{aligned} H_{SSH} &= -\textstyle\sum_{i=1}^{N-1} \left[[t + (-1)^i 2\alpha u](c_{i+1}^\dagger c_i + c_i^\dagger c_{i+1}) \right. \\ &\quad \left. \frac{K}{2}(-2(-1)^n u)^2 + \frac{M}{2}(-1)^n \dot{u}^2 \right] \end{aligned} \quad (15)$$

where α denotes the electron-phonon coupling, and K is the spring constant of the phonon.

The quantum simulation of the SSH model with 2 fermions (due to qubit limit of 5) and a single boson is shown in Figure 17 with a quantum depth of 5, and 1024 shots over which the value was averaged with a percent error of 205.57 %.

Percent error in the ground state energy value given by the VQE plotted versus the number of shots over which the values averaged for simulations of the SSH model of two fermions and one boson using a quantum depth of 3 are shown in Figure 15, showing that increasing the number of shots reduces the percent error, however, the VQE fails to converge to the exact value of the ground state energy of the Hamiltonian.

The quantum simulation of a tight-binding model for a ring of 5 atoms is shown in Figure 16 with a percent error of 40.61 %.

For the case of a single boson with effective action, the free energy as a function of flux given by:

Fig. 16: Quantum simulation for ground state energy of a N=5 carbon nanoring.

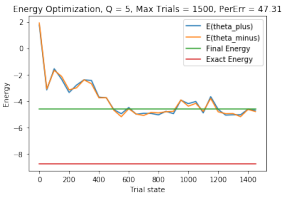

Fig. 17: SSH model of polyacetylene on the IBM Quantum simulator.

$$F_{ferm,bos} = \pm kT \sum_i \ln(1 \pm \exp(-\omega_i/kT)) \tag{16}$$

modeled instead as a function of u, the scalar field matrix representing boson and with a term for potential, the flux potential $V(u)$ is interpolated and modeled using Mathematica in Figure 22.

The quantum simulation of a single boson in the SSH model is shown in Figure 18.

C. Four fermion interaction

The four-fermion interaction gives a description for local interactions between four fermions at a single spacetime point. The Gross-Neveu model of four-fermion interactions in (1+1) time and spacial dimensions for N self-coupled Dirac fermions is given by the Lagrangian density:

$$\mathcal{L} = \overline{\psi}_a(i\not{\partial} - m)\psi^a + \frac{g^2}{2N}[\overline{\psi}_a\psi^a] \tag{17}$$

where ψ_a ($\overline{\psi}^a$) is the Dirac fermion (the Dirac adjoint $\overline{\psi} = \psi\gamma^0$), g is the coupling constant, N is the number of Dirac fermions, and $\not{\partial}$ is $\gamma^\sigma\partial_\sigma$.

The low energy effective continuum theory of the Gross-Neveu model, evaluated with degrees of freedom phonon can be represented as

$$\mathcal{L} = \overline{\psi}(i\gamma^\mu\partial_\mu\psi) - \frac{1}{2}\sigma^2 - g\sigma\overline{\psi}\psi \tag{18}$$

The Hamiltonian for the *trans*-polyacetylene modeled by the Gross-Neveu model is given by [22]:

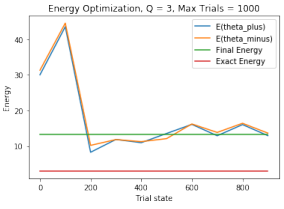

Fig. 18: SSH model of single boson on IBM Quantum Simulator.

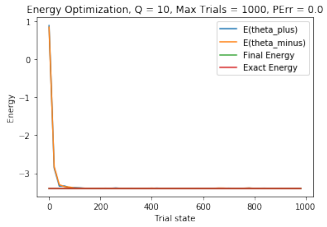

(a) Gross Neveu Model polyacetylene with Four Fermions

Fig. 19: Quantum Simulation of the Gross-Neveu model of 4 fermions on a *trans*-polyacetylene chain

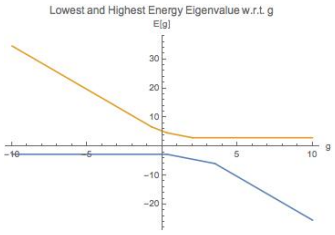

(a) E vs. g

Fig. 20: Largest and Smallest energy eigenvalues of the Gross-Neveu model as a function of g.

$$H = H_0 + H_g + H_W$$

$$H_0 + H_W = \sum_{i=1}^{N}\sum_p \tfrac{1}{L}E_k(a_i^\dagger(p)a_i(p) + b_i^\dagger(p)b_i(p))$$
$$H_g = -\tfrac{g^2}{2}\sum_x a\Big(\sum_{i=1}^{N}\bar{\psi}_i(\mathbf{x})\psi_i(\mathbf{x})\Big)^2$$

where; (19)

$$\psi_i(x) = \sum_p \tfrac{1}{L}\tfrac{1}{E_p}\Big(a_i(p)u(p)e^{ip\cdot x} + b_i^\dagger(p)v(p)e^{-ip\cdot x}\Big)$$
$$\bar{\psi}_i(x) = \sum_p \tfrac{1}{L}\tfrac{1}{E_p}\Big(a_i^\dagger(p)\bar{u}(p)e^{-ip\cdot x} + b_i(p)\bar{v}(p)e^{ip\cdot x}\Big)$$
$$u(p) = \begin{bmatrix}\sqrt{E_p - p}\\ i\sqrt{E_p - p}\end{bmatrix}, v(p) = \begin{bmatrix}\sqrt{E_p - p}\\ -i\sqrt{E_p - p}\end{bmatrix}$$

and the bar over a symbol represents its dot product with the second Pauli matrix. Mapping the Hamiltonian to qubits is performed on Mathematica [23].

Modeled as

$$H = -\sum_{j=1}^{N} t(c_j^\dagger c_j) - \sum_{j=1}^{N-1} g(c_{j+1}^\dagger c_{j+1} c_j^\dagger c_j) \tag{20}$$

for c_j ($c_j^\dagger$) annihilate (create) a fermion at site j. When simulated on the quantum computer, the eigensolver converged to the exact value within fewer than a 0.01 percent error for a value of g = 0.1.

D. VQE with Effective Potential

The Variational Quantum Eigensolver is an important tool for quantum chemistry using the Quantum Computer. It effectively solves the Schrödinger equation of a non-trivial Hamiltonian of a molecule. It performs an unconstrained energy optimization in the Fock space of the original electronic problem. The solution contains information important to understanding the properties of the molecular system. With increasing numbers of interacting particles (electrons) the system becomes exponentially more difficult to solve on classical computer, motivating its use on the quantum computer.

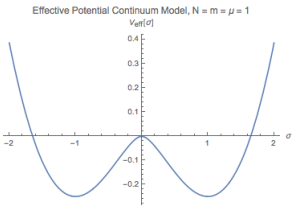

Fig. 21: Effective Potential for the continuous case as a function of σ.

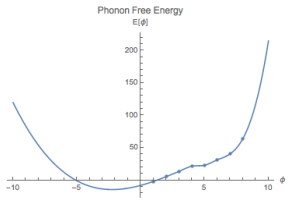

Fig. 22: Phonon Free Energy – substitution of phonon for flux with a momentum term

The two basic steps leading up to the VQE algorithm are mapping between fermionic and qubit operators and factoring the effective Hamiltonian into Pauli matrices.

Using Mathematica code, the the Hamiltonian is represented as $H = \sum_i d_i P_i$ where the d_i are coefficients given by $d_i = \frac{1}{N} Tr(HP_i)$ and P_i are Pauli Matrices.

The Variational Quantum Eigensolver approach is dependent on a good 'trial' state.

The quantum computer prepares variational trial states based on parameters, and the expectation value of the energy is estimated and then used in a classical optimizer to generate improved parameters [24]. For its default optimization algorithm IBM uses simultaneous perturbation stochastic approximation (SPSA).

The trial state is prepared by applying an ryrz circuit supplied by the SPSA optimization module. Theoretically, any state can be built from the ground state by applying a series of R_y and R_z rotations [25]. Measurements of the Hamiltonian are taken as each qubit state is put into a superimposed state by the application of a Hadamard gate followed by the R_y and R_z rotations.

The VQE uses the variational principle to calculate the upper bound of the ground energy state of a system.

Effective potential accounts for the quantum fluctuations in the classical potential of a system. The effective potential rewrites the effect of fermion fields in terms of boson fields, and reduces the degrees of freedom for the system. The ground state of the Gross Neveu model of a 2D lattice is given by the minimum of the effective potential [26].

The Gross Neveu model with chemical potential using the large-N approximation seen in Figure 21 has a 1/N expansion of

$$\begin{aligned} V_eff(\sigma) &= \frac{\sigma^2}{2N} + \frac{\sigma^2}{4N}\Big[\theta(\sigma^2-\gamma^2)\ln(\tfrac{\sigma^2}{\sigma_0^2}-3) \\ &\quad +\theta(\gamma^2-\sigma^2)2\ln(\tfrac{\gamma+\sqrt{\gamma^2-\sigma^2}}{\sigma_0}-3)\sigma_0^2-3) \\ &\quad -\tfrac{\gamma}{2N}\sqrt{\gamma^2-\sigma^2}\theta(\gamma^2-\sigma^2) \end{aligned} \tag{21}$$

where $\gamma = \mu\sqrt{N/\pi}$, σ is an auxiliary field representing boson degrees of freedom, μ is the chemical potential, and $\theta(x)$ is the Heaviside step function [27].

IV. Conclusion

Over the course of this project we created several visualizations of discrete quantum systems with interesting topologies. The models visualized included twisted bilayer graphene for various twist angles, pentagonal cones and nanohorns, as well as nanostrip rings and Möbius strips using open-source molecular modeling software. The adjacency matrices and tight binding models were used to generate the energy dispersion relations and free energy of the models. The propagator, and entanglement entropy of the one-dimensional model of a ring composed to carbon atoms were modeled using Mathematica. The nanoring and polyacetylene ground state energies were modeled on the IBM Quantum Experience simulator, with large percent errors for the converged values for the Su-Schrieffer-Heeger model with phonon interaction, and a simple tight binding model with nearest neighbor hopping. The Gross-Neveu model simulated on the quantum simulator converged to the ground state energy. While quantum computing shows much promise in completing complex calculations, there are still many issues with scalability and decoherence. In order to perform the factorization of the Hamiltonian, the VQE requires the ability to create the Hamiltonian in matrix form. For Hamiltonians of increasing complexity this will become more and more difficult to achieve on a classical computer. The size of the system that can be modeled is also limited by the number of qubits available for mapping. Additionally, the rxry-trial circuit used to prepare the trial state was not appropriate for each model studied. Determining a trial-circuit for each model presents a complicated obstacle to using the Variational Quantum Eigensolver in complex models. The trial wavefunctions used are likely too close to the values for the excited states, suggested by the simulations failing to converge to the ground state energy value.

V. Acknowledgements

I would like to thank my research mentor Dr. Michael McGuigan for his time and effort to introduce me to these topics and direct my focus. I would also like to thank Aditya Samaroo, Brandon Ortega and Huub van Dam for their valuable discussions. This project was supported in part by the U.S. Department of Energy, Office of Science, Office of Workforce Development for Teachers and Scientists (WDTS) under the Science Undergraduate Laboratory Internships Program (SULI). We acknowledge use of the IBM Q for this work. The views expressed are those of the authors and do not reflect the official policy or position of IBM or the IBM Q team.

References

[1] M. D. Hanwell, D. E. Curtis, D. C. Lonie, T. Vandermeersch, E. Zurek, and G. R. Hutchison, "Avogadro: an advanced semantic chemical editor, visualization, and analysis platform," in *J. Cheminformatics*, 2012.

[2] W. Humphrey, A. Dalke, and K. Schulten, "VMD – Visual Molecular Dynamics," *Journal of Molecular Graphics*, vol. 14, pp. 33–38, 1996.

[3] J. Stone, J. Gullingsrud, P. Grayson, and K. Schulten, "A system for interactive molecular dynamics simulation," in *2001 ACM Symposium on Interactive 3D Graphics*, J. F. Hughes and C. H. Séquin, Eds. New York: ACM SIGGRAPH, 2001, pp. 191–194.

[4] A. H. Castro Neto, F. Guinea, N. M. R. Peres, K. S. Novoselov, and A. K. Geim, "The electronic properties of graphene," *Rev. Mod. Phys.*, vol. 81, pp. 109–162, Jan 2009. [Online]. Available: https://link.aps.org/doi/10.1103/RevModPhys.81.109

[5] K. S. Novoselov, A. K. Geim, S. V. Morozov, D. Jiang, Y. Zhang, S. V. Dubonos, I. V. Grigorieva, and A. A. Firsov, "Electric Field Effect in Atomically Thin Carbon Films," *Science*, vol. 306, pp. 666–669, Oct. 2004.

[6] J. Xue, "Scanning probe microscopy of graphene and carbon nanotubes," 07 2018.

[7] D. Gunlycke and C. T. White, "Tight-binding energy dispersions of armchair-edge graphene nanostrips," *Phys. Rev. B*, vol. 77, p. 115116, Mar 2008. [Online]. Available: https://link.aps.org/doi/10.1103/PhysRevB.77.115116

[8] Y. Cao, V. Fatemi, S. Fang, K. Watanabe, T. Taniguchi, E. Kaxiras, and P. Jarillo-Herrero, "Unconventional superconductivity in magic-angle graphene superlattices," *Nature*, vol. 556, pp. 43–50, Apr. 2018.

[9] A. Samaroo and M. McGuigan, "Using ibm-q to study and visualize the ground state properties of the su-schrieffer-heeger model," 2018.

[10] T. Duong and M. McGuigan, "Visualization of higher genus carbon nanomaterials: free energy, persistent current, and entanglement entropy," pp. 1–5, Aug 2017.
[11] C. P. Herzog and T. Nishioka, "Entanglement entropy of a massive fermion on a torus," *Journal of High Energy Physics*, vol. 3, p. 77, Mar. 2013.
[12] J.-C. Charlier and G.-M. Rignanese, "Electronic structure of carbon nanocones," *Phys. Rev. Lett.*, vol. 86, pp. 5970–5973, Jun 2001. [Online]. Available: https://link.aps.org/doi/10.1103/PhysRevLett.86.5970
[13] P. E. Lammert and V. H. Crespi, "Topological Phases in Graphitic Cones," *Physical Review Letters*, vol. 85, pp. 5190–5193, Dec. 2000.
[14] V. A. Osipov and E. A. Kochetov, "Dirac fermions on graphite cones," *Journal of Experimental and Theoretical Physics Letters*, vol. 73, no. 10, pp. 562–565, May 2001. [Online]. Available: https://doi.org/10.1134/1.1387528
[15] D. V. Kolesnikov and V. A. Osipov, "Electronic structure of carbon nanohorns near the fermi level," *Journal of Experimental and Theoretical Physics Letters*, vol. 79, no. 11, pp. 532–536, Jun 2004. [Online]. Available: https://doi.org/10.1134/1.1787100
[16] R. Feynman, A. Hibbs, and D. Styer, *Quantum Mechanics and Path Integrals*, ser. Dover Books on Physics. Dover Publications, 2010. [Online]. Available: https://books.google.com/books?id=JkMuDAAAQBAJ
[17] H. A. Weldon, "Chemical potentials in real-time thermal field theory," *Phys. Rev. D*, vol. 76, p. 125029, Dec 2007. [Online]. Available: https://link.aps.org/doi/10.1103/PhysRevD.76.125029
[18] A. Niégawa, "Comment on Fermion Propagator in Real-Time Quantum-Field Theory at Finite Temperature and Density," *Modern Physics Letters A*, vol. 17, pp. 303–308, 2002.
[19] M. Lutz and T. Kunihiro, "Causal structure of the thermal propagator in real-time formalisms," *Zeitschrift für Physik C Particles and Fields*, vol. 49, no. 1, pp. 123–127, Mar 1991. [Online]. Available: https://doi.org/10.1007/BF01570803
[20] J. K. Asbóth, L. Oroszlány, and A. Pályi, "A Short Course on Topological Insulators: Band-structure topology and edge states in one and two dimensions," *ArXiv e-prints*, Sep. 2015.
[21] Y. Kobayashi and H. Minakata, "Thermodynamics of the Su-Schriefer-Heeger model," 1994.
[22] S. P. Jordan, K. S. M. Lee, and J. Preskill, "Quantum Algorithms for Fermionic Quantum Field Theories," *ArXiv e-prints*, Apr. 2014.
[23] A. Hamed Moosavian and S. Jordan, "Faster Quantum Algorithm to simulate Fermionic Quantum Field Theory," *ArXiv e-prints*, Nov. 2017.
[24] A. Kandala, A. Mezzacapo, K. Temme, M. Takita, M. Brink, J. M. Chow, and J. M. Gambetta, "Hardware-efficient variational quantum eigensolver for small molecules and quantum magnets," *Nature*, vol. 549, pp. 242–246, Sep. 2017.
[25] V. V. Shende, S. S. Bullock, and I. L. Markov, "Synthesis of quantum-logic circuits," *IEEE Transactions on Computer-Aided Design of Integrated Circuits and Systems*, vol. 25, no. 6, pp. 1000–1010, June 2006.
[26] T. Izubuchi, J. Noaki, and A. Ukawa, "Two-dimensional lattice Gross-Neveu model with Wilson fermion action at finite temperature and chemical potential," *Phys. Rev. D.*, vol. 58, no. 11, p. 114507, Dec. 1998.
[27] H. Minakata and A. Chodos, "The Gross-Neveu Model with Chemical Potential; An Effective Theory for Solitonic-Metallic Phase Transition in Polyacetylene?" *ArXiv High Energy Physics - Theory e-prints*, Sep. 1997.